Microscopic modeling and simulation of transverse-mode dynamics of vertical-cavity surface-emitting lasers

C. Z. Ning and P. M. Goorjian

*Computational Quantum Optoelectronics, NASA Ames Research Center, N229-1,
Moffett Field, California 94035-1000*

The dynamics of transverse modes of vertical-cavity surface-emitting lasers were simulated by use of a model that incorporates microscopically computed gain and refractive index with many-body effects. The model equations were solved by finite-difference methods in two-dimensional space and time domains without any *a priori* assumptions of symmetry of solutions or types and number of modes. Simulation was carried out for devices with and without index guiding at various pumping levels. We show that index-guided vertical-cavity surface-emitting lasers involve more transverse modes than purely gain-guided devices at the same pumping level. Both time-resolved and time-averaged near-field patterns over several time scales are investigated. Complicated spatial and temporal dynamic behaviors occur at higher pumping levels that include azimuthal rotating waves and intensity oscillations owing to dynamic competition between modes of the same order and those of different orders. © 1999 Optical Society of America [S0740-3224(99)00311-2]

OCIS codes: 250.7260, 140.5960, 140.2020, 250.0250, 140.0140.

1. INTRODUCTION

Vertical-cavity surface-emitting lasers (VCSEL's) are becoming increasingly important for an ever-widening range of applications that range from optical interconnects, optical storage, and CD reading–writing systems to various medical diagnostics. More new applications emerge continually as new wavelength VCSEL's become available and their performance improves.[1,2] Beam quality or transverse-mode behavior is very important for many of current and potential applications. As a result, the issue of transverse modes of VCSEL's has received extensive attention and is still a topic for active experimental[3–19] and theoretical[20–39] investigations. More specifically, transverse modes of VCSEL's are important for (1) high-power VCSEL's, for which multiple transverse modes occur as the result of a large transverse area,[13,18,19] high pumping, or both, (2) multimode fiber data links,[10,11] for which it was shown that multimode VCSEL's lead to reduced modal noise, (3) modulated VCSEL's for which multiple transverse modes affect the modulation bandwidth or lead to a double-peaked response,[4–6] (4) feedback from the application interfaces, for which multiple transverse modes are shown to lead to distance-dependent coupling efficiency,[15] and (5) applications in which selected transverse modes are desired or engineering of certain near or far-field patterns is necessary.[18,19]

Experimentally, multiple transverse modes have been analyzed in various ways, including spectrally resolved near-field measurement,[3–6,13,14,35] polarization-resolved near-field measurements,[3,35] and spatially and spectrally resolved spontaneous emission near-field,[9] and time-resolved near-field imaging.[11] One additional new method is scanning near-field optical microscopy, which permits spatially resolved spectroscopic measurements to be made.[16,17] Such spatially resolved spectra can be used to reconstruct transverse-mode patterns according to the spectral content of each mode for a given pumping. VCSEL emissions at the output facets[16] and along the VCSEL cavity[17] have been measured by this method. As a result of such detailed experiments, quite extensive experimental data have been accumulated, and many interesting phenomena have been observed.

Theoretically or in terms of numerical simulation, research activities carried out until now can be characterized as follows: First, many simulations have computed passive and static transverse modes[26–34] for vector or scalar fields. Such simulations often treat VCSEL structures in the plane of or vertical to semiconductor layers, including oxidation layers and mirror stacks, in great detail. This type of simulation is helpful for predicting possible mode structures and for determining threshold and mode spacing of the transverse modes. The disadvantage of such an approach is also obvious: Because the models are passive and static, meaning that self-consistent couplings to the gain material and time evolution of transverse modes are not included, the models cannot predict spatial hole-burning effects and dynamic mode competition when multiple modes are involved. The second type of approach includes self-consistent couplings between optical fields and gain media.[20–25] Time evolution of both material and laser field variables is also considered. The advantages of the second approach compared with the first one is obvious. The disadvantage is that it usually requires a determination of the number and type of modes *a priori*. Usually lower orders of the Gauss–Hermite (for rectangular VCSEL's) or Gauss–Laguerre (for circular VCSEL's) modes are chosen. Of-

ten in such simulations only a few modes and those with azimuthal symmetry are chosen for the sake of simplicity. Inasmuch as a transverse definition of gain- or index-guided VCSEL's is far from that of a typical ideal waveguide, the modes obtained under ideal boundary conditions should be used with caution, especially when only a few modes are used. Another related issue in this approach is the treatment of the beating terms in the carrier-density equation that result from mode decompositions. To the best of our knowledge, all the papers mentioned above ignore the temporal and spatial beating terms. Although an argument can be made to support neglecting spatial beating terms because of long carrier diffusion length, temporal beating should be carefully examined, especially for those modes that are not far apart in the frequency domain.

Another crucial element in modeling any semiconductor laser is the treatment of the gain medium. In most of the current works, gain and refractive index have been treated by a linear gain coefficient and by the so-called alpha factor.[40,41] As was pointed out elsewhere,[42,43] there are several limitations to such an approach. These include the neglect of the nonlinear carrier density dependence and of the wavelength dependence of gain and refractive index. To describe broad-area lasers and lasers with many longitudinal or transverse modes for which carrier-density and wavelength dependence of the gain is important, a set of equations, called effective Bloch equations (EBE's), was derived.[42] This set of equations has been applied to simulation of broad-area edge-emitting lasers[43–47] and recently to VCSEL's.[37,38]

In this paper we attempt to overcome some of the shortcomings of the VCSEL modeling and simulations mentioned above. We apply the EBE's[42] to VCSEL's by projecting out the longitudinal mode and keeping only the transverse space dependence. The approach that we describe here is similar in spirit to that of Ref. 37 in which plasma heating and thermal effects were also included but many-body effects were not considered. The resultant partial differential equations are solved directly by finite-difference methods in two-dimensional (2D) space and time domains. The outline of this paper is as follows: In Section 2 we present the basic equations and describe the gain materials and the gain model. In Section 3 we present the results of our numerical simulation and consider devices of different sizes, with and without index guiding. We compare the cases with and without index guiding to study the effects of index guiding. Both time-resolved and time-averaged near-field patterns are studied. We then conclude this paper by summarizing the main results and making some remarks.

2. BASIC EQUATIONS

The model that we use in this paper is the EBE's,[42] which are constructed from the microscopic theory[48] with many-body effects included. This model was used recently for investigation of the transverse-mode dynamics of high-power broad-area lasers and lasers with integrated amplifiers.[37,43,46,47,49] The details of the construction and limitation of this model have been extensively discussed elsewhere.[42,43,49] To apply this model to VCSEL's, we no-

tice that VCSEL's have short and high-finesse cavities that define sharp and well-separated longitudinal-mode resonances. This fact allows us to project the spatial dependence of the laser field along the propagation direction and to introduce a longitudinal confinement factor (denoted Γ in what follows), as was also done previously.[39,50] The resulting EBE's for VCSEL's can be written as follows:

$$\frac{n_g}{c}\frac{\partial E}{\partial t} = \frac{i}{2K}\nabla_\perp^2 E - \kappa E + i\frac{\delta n(x, y)K}{n_b}E$$
$$+ \frac{iK\Gamma}{2\epsilon_0\epsilon_b}(P_0 + P_1), \qquad (1)$$

$$\frac{\partial P_1}{\partial t} = \{-\Gamma_1(N) + i[\delta_0 - \delta_1(N)]\}P_1$$
$$- i\epsilon_0\epsilon_b A_1(N)E, \qquad (2)$$

$$\frac{\partial N}{\partial t} = \nabla_\perp D_N \nabla_\perp N - \gamma_n N + \frac{\eta J(x, y)}{e}$$
$$+ i\frac{L\Gamma}{8\hbar}[(P_0 + P_1)^*E - (P_0 + P_1)E^*], \quad (3)$$

where $P_0 = \epsilon_0\epsilon_b\chi_0(N)E$.

The variables and parameters are defined as follows: E is the slowly varying complex amplitude of the laser field, and N is the 2D carrier density. P_0 and P_1 are complex polarizations of the semiconductor medium induced by the laser field. n_g and n_b are the group and the phase refractive indices of the unexcited semiconductor. c is the speed of light, and ϵ_0 is the dielectric constant, both for vacuum. $K = 2\pi n_b/\lambda$ is the optical wave vector in the medium, where λ is the wavelength. γ_n is the carrier decay rate. κ is the loss that is due to cavity transmission and background absorption; it is related to the corresponding decay rate $\tilde{\kappa}$ through $\kappa = \tilde{\kappa}n_g/c$. The value of $\tilde{\kappa}$ is taken as 0.52/ps in this paper. $\nabla_\perp$ represents spatial derivatives with respect to x and y, which are transverse to the propagation direction. δ_0 is the detuning between the reference and the bandgap frequencies. The diffusion constant is taken as $D_N = 20\,\text{cm}^2/\text{s}$, and the carrier decay constant is assumed to have a value of 1 ns^{-1}. Cavity length L is one half of the wavelength. $\delta n(x, y)$ in the third term in Eq. (1) defines the index confinement profile, which can represent any engineered index confinements, such as those that are due to oxidation. The gain confinement is represented by the space-dependent current profile $J(x, y)$.

We note that there are a few coefficients in Eq. (2), such as Γ_1, δ_1, A_1, and $\chi_0 = \chi_0' + i\chi_0''$. These are carrier-density dependent. As can easily be seen from Eq. (2), the first three parameters define a Lorentzian-type oscillator. The strength A_1, the width Γ_1, and the resonance frequency δ_1 from the reference frequency determine the gain bandwidth and the gain change with carrier density. The density dependence of these parameters makes the set of equations different from the standard two-level Bloch equations.
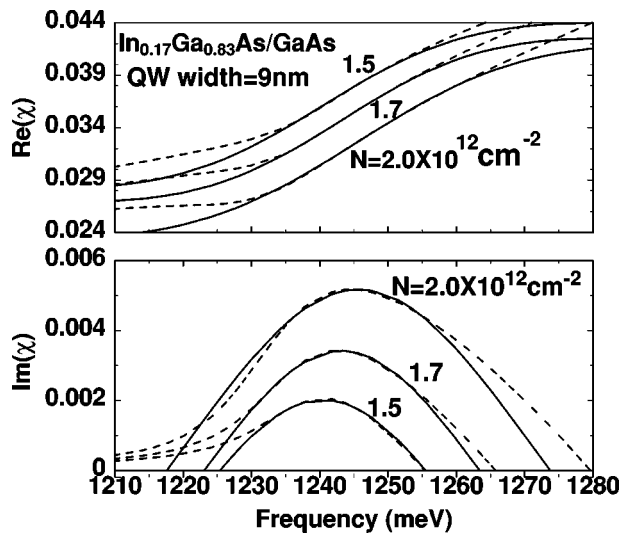
Fig. 1.   Real and imaginary parts of optical susceptibility (χ) for three carrier densities computed from the microscopic theory (dashed curves) and fitted with the effective Lorentzian parameters (solid curves).   QW, quantum well.

For a given quantum-well structure, a first-principle theory calculation is carried out with a detailed model that includes all the important many-body effects, such as bandgap renormalization, Coulomb enhancement, and the line shape of optical transitions.   The line shape is treated with detailed scattering terms at the second order of Coulomb potential.[49,51–53]   Such treatment of the scattering terms has been shown to be important in producing the correct gain shape.[49,51–53]   As we have pointed out in the past, the significant aspects of this model its the capability to include the carrier-density dependence of gain and refractive index through those Lorentzian parameters and the wavelength dependence of gain through time evolution of an effective polarization P_1.   The wavelength dependence of optical gain has been ignored in laser modeling, with only a few exceptions.[54]   We point out that this dependence is quite important for multiple-transverse-mode operation, because the mode space is in the range from tens to hundreds of gigahertz,[3] as we shall also see in what follows.   Another interesting case for which the wavelength dependence of optical gain is important is that of VCSEL arrays with engineered multiple wavelengths,[55,56] for which the wavelength spans more than 20 nm.   The gain difference across such a large frequency range is obviously significant in determining the outcome of the mode competition.

In this paper we consider an active region consisting of four $In_{0.17}Ga_{0.83}As/GaAs$ quantum wells, each 9 nm thick. Figure 1 shows the spectra of gain and refractive index for this structure at three excitation levels computed from the microscopic theory (dashed curves).   The solid curves represent Lorentzian fittings.   The fittings determine the five density-dependent Lorentzian coefficients.   Once these coefficients are determined, the heterostructure and band-structure information of a given laser is then contained in the EBE's.   Numerical solution of these EBE's will allow us to simulate and predict laser output, using the accurate information of the quantum structure and material compositions.

3.   NUMERICAL RESULTS

Instead of making mode decomposition, we solve the EBE's by finite-difference methods in space and time domains directly.   In our simulation we use 101 grid points in both the x and the y directions over a square computation domain of 30 μm.   Use of this computation domain ensures that the field practically vanishes at the boundary of the computation domain for the devices sizes that we consider in this paper.   In the simulations described in what follows, we consider gain-guided VCSEL's and gain- and index-guided VCSEL's.   Gain guiding is determined by the pumping profiles or the current contact. We have considered two contact shapes in our simulation: disk and ring shapes: All these profiles are shown in Fig. 2 for a device 15 μm in diameter.   Note also that we use smoothed edges for all index or current profiles, instead of sharp edges, to mimic the carrier diffusions at the edges or oxidation profiles.   The smoothness of these edges will also affect device performance and is one aspect of device engineering.   In this paper, the values of pumping current and guiding refractive index refer to their values in the flat region (maximum value) in Fig. 2.   For pumping current we use $J_0 = 1$ kA/cm^2 as the measuring unit.

A.   Dynamics of Gain-Guided Device
The first device of our simulation is one with a circular active region 7.5 μm in diameter without additional index guiding [$\delta n(x, y) = 0$].   The threshold of this device is near $J = 0.6 J_0$.   Immediately above threshold the VCSEL shows a stable fundamental mode.   When the pumping current increases to $0.7 J_0$ the device becomes unstable.   Snapshots of near-field patterns are shown in Fig. 3 for this pumping level.   Figures 3a–3d show four different orientations of the first-order modes.   Because of the cylindrical symmetry[20] of the device, all orientations are in principle possible.   We have indeed seen over a time interval of a few nanoseconds different orientations of this first-order mode.   Figures 3e–3h show the single peak located at different sites in the device.   From the animation of the near-field evolution we see that the device shows two types of motion: a rotating-wave type of motion involving two peak patterns and an antiphase type of competition between the two peaks.   Figures 3e–3h actually show those moments in time when one of the two peaks disappears and the other peak reaches its maximum intensity.   This competition results in antiphase oscillation of the two peaks at one given orientation.   After a few cycles of such oscillations, the system
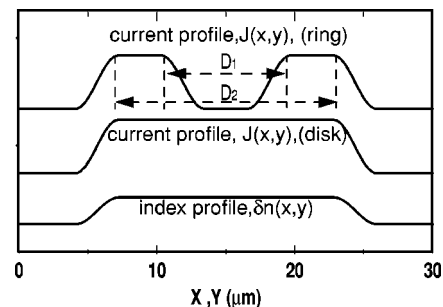

Fig. 2.   Index confinement and pumping current profiles (gain guidings) for disk- and ring-shaped contacts.
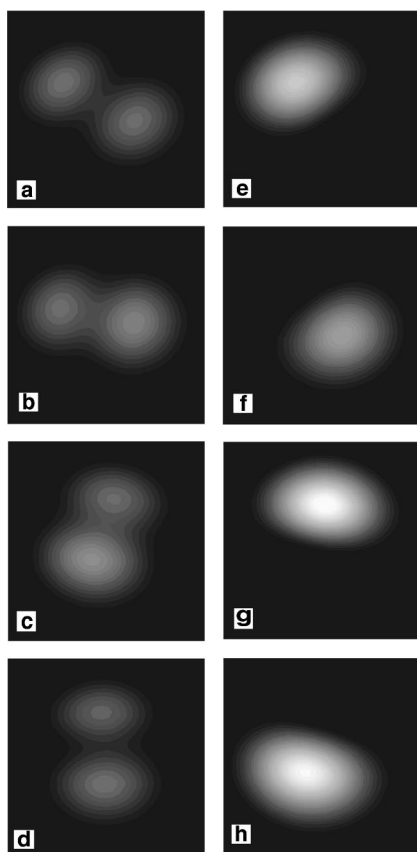
Fig. 3. Snapshots of the near-field patterns at eight different moments for a gain-guided VCSEL 7.5 μm in diameter at J = $0.7J_0$.

rotates to another orientation and performs the antiphase oscillations there. The mechanism behind such dynamics is the mode beating between the zeroth- and the first-order modes, which results in fast intensity oscillations, and between the first-order modes of different orientations, which induces the rotating waves.

To look at such dynamic behavior from a complimentary perspective, we record the time evolution of the local field at five different positions in the transverse plane. The locations are shown in the inset at the top of Fig. 4 and are denoted t (top), b (bottom), r (right), l (left), and c (center). The corresponding time series are shown in the three parts of the figure. We also take a spatial average signal, which is denoted by the letter a. We see that time series at all five locations and the average all show basically similar types of oscillation, with gross features showing fast and slow oscillation. These two oscillations are more visible in the average signal. Another feature is that there are time windows where top and bottom signals (or right and left signals) show antiphase oscillations, as can be seen clearly from the middle set of curves row and from the right-hand part of the bottom set of curves. This behavior corresponds to the fast intensity alternations of the two peaks at a given orientation, as we mentioned above.

The power spectra for those local fields are shown in Fig. 5. We see that all six data sets show similar spectra, with some differences in the fine features. The second group of peaks appears near 90 GHz, which is the fre-

quency splitting between the zeroth- and first-order modes, and this shows that the two peak oscillations involve the beating of the zeroth- and first-order modes. We also see such involvement of the zeroth-order mode in the animation of the time evolution. The spatially resolved spectra provide a useful way to compare simulation results with experimental measurements when direct spatially resolved spectral-domain measurements have already been carried out for VCSEL's.[16] We intend to attempt a detailed comparison in the future.

When the pumping is further increased to $1.5J_0$, the near-field patterns become more complicated. Figure 6 shows snapshots of the near-field evolution at this pumping level. We still see mainly zeroth- and first-order modes. But now the first-order modes becomes severely
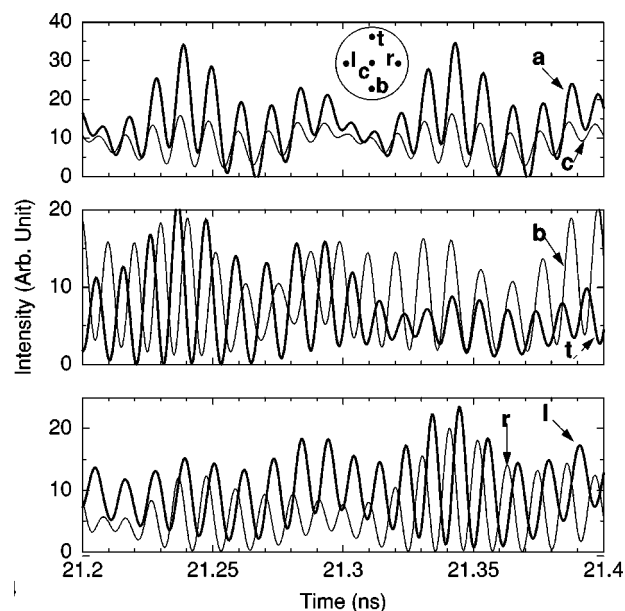

Fig. 4. Time evolution of the local field for the gain-guided 7.5-μm VCSEL at $J = 0.7J_0$. The five locations are indicated in the inset.
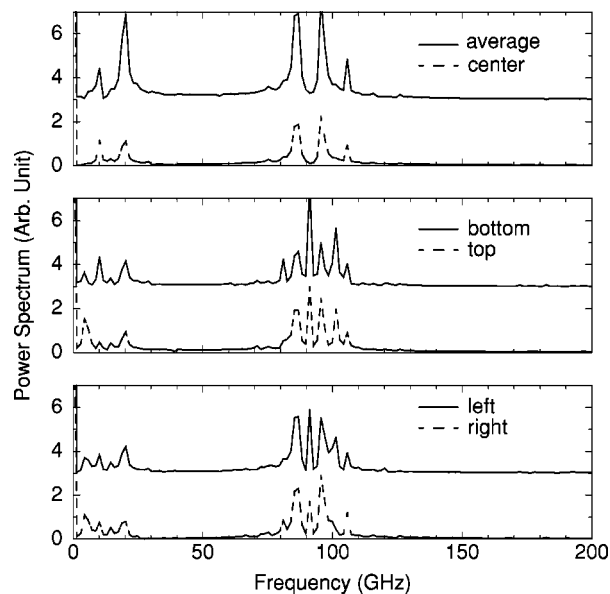

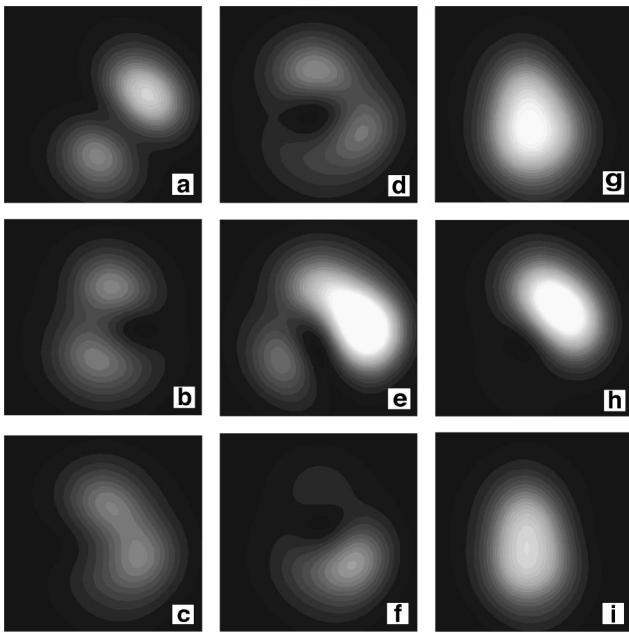Fig. 5. Power spectra for the local fields and the average field presented in Fig. 4.

Fig. 6.   Snapshots of the near-field patterns at nine moments for a gain-guided VCSEL 7.5 μm in diameter at $J = 1.5 J_0$.

distorted.   The component of zeroth-order mode (one center spot) is stronger, as indicated in Figs. 6g–6i.   This means stronger competition between modes of the the two orders, with each of them modified by the other.   As a result, all the two-peak patterns (Figs. 6a–6f) are different from the pure TEM_{01}/TEM_{10} modes.   Here again as in the previous case, the dominant feature is the rotating-wave motions and oscillations of peak heights.   However, the two types of motion now alternate more irregularly. The more remarkable differences from the previous case are shown in Fig. 7, where time series [Fig. 7(a)] and spectra [Fig. 7(b)] of the averaged and center signals are plotted.   Time series a and c are both apparently chaotic. The spectra are indeed a quasi-continuum, indicating that the signals are indeed chaotic.   The fact that only a few lower-order modes are involved in this temporal chaos is due to the small device size and the relatively large mode spacings.

B.   Effects of Index Guiding
We now add index guiding to the device of the last subsection.   The index profile $\delta n(x, y)$ is zero within the active region and smoothly ramped down to -0.05.   Thus the maximum index step is 0.05.   This number corresponds to a modal index change introduced by an oxidation layer outside the active region.[36]   Figure 8 shows snapshots of the near field at $J = 0.7 J_0$, the same level as in Figs. 3–5.   In Fig. 8 we see that two- (Figs. 8a–8c), three- (Figs. 8d–8i), and four-peak (Figs. 3j–3l) patterns are all evident, including different orientations of two- and three-peak patterns.   Figure 9 shows the time evolution of the local field at the five locations mentioned above and of the average field.   First, we notice that the average field is much more regular than those of the other five data sets, with a quite regular slow oscillation superimposed upon a fast oscillation of tiny amplitude.   Second, we see that the larger-amplitude oscillations of the top

and bottom (or right and left) data sets are in antiphase. These two features are both due to the better phase relationships between the transverse modes with index guiding than without.   As a result of good phase relations, the destructive interference of different transverse modes leads to a simple, regular oscillation of the average field. This understanding is also supported by the spectral data shown in Fig. 10.   We see that the left and right (or top and bottom) data sets have the same spectral components, whereas the average field has only one frequency
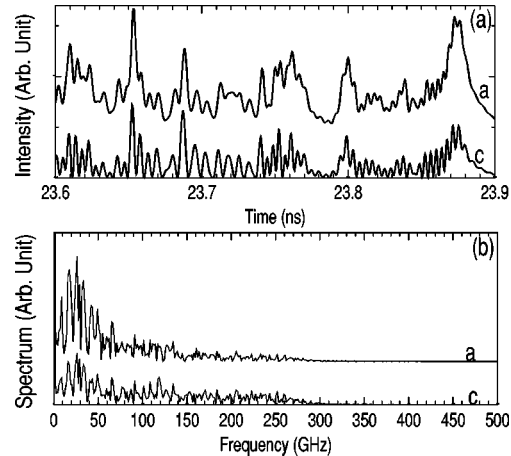

Fig. 7.   (a) Time evolution and (b) power spectra for the local fields and the average field presented in Fig. 6.
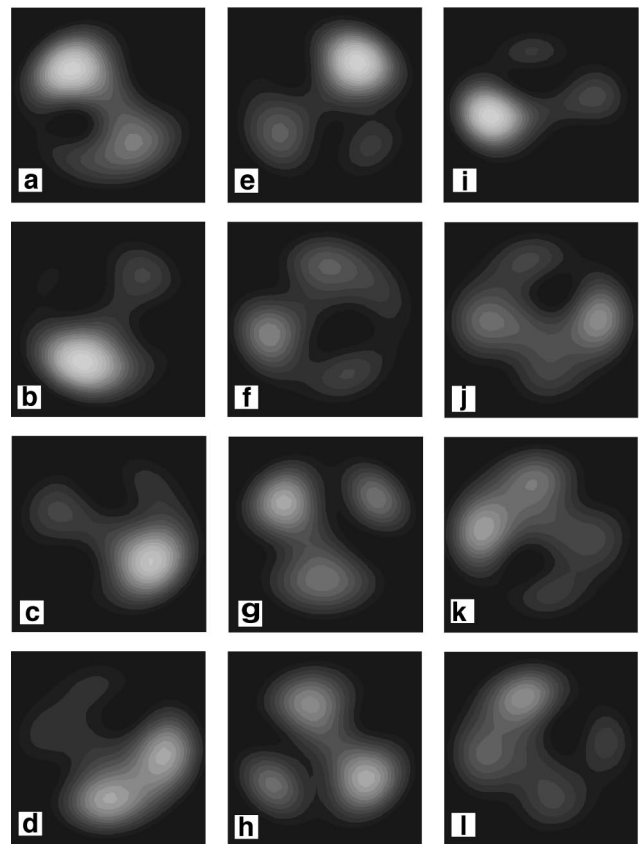

Fig. 8.   Snapshots of the near-field patterns at 12 different moments for a gain- and index-guided VCSEL 7.5 μm in diameter at $J = 0.7 J_0$.
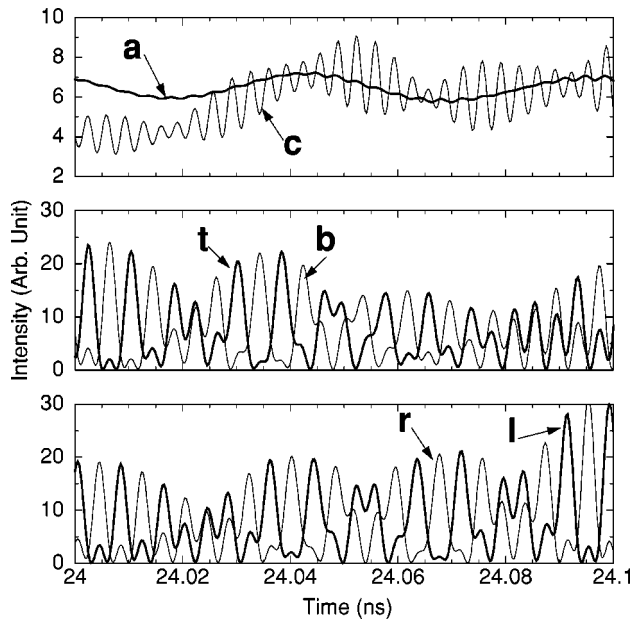
Fig. 9. Time evolution of the local fields and of the average field for the VCSEL of Fig. 8a. Letters a, c, t, b, r, and l have the same meanings as in Fig. 4.
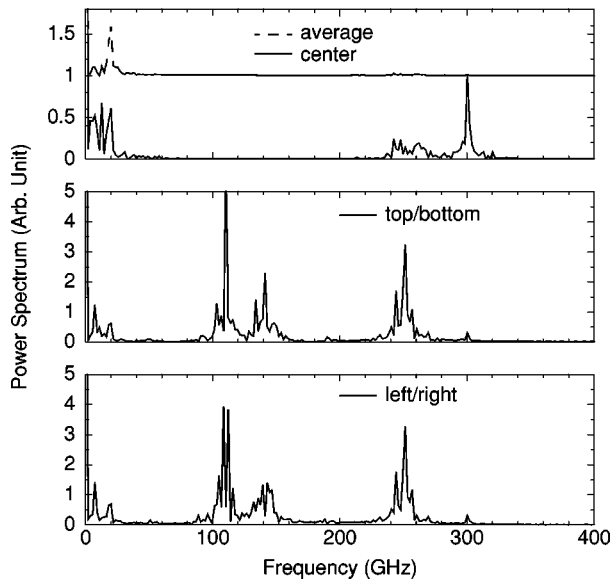

Fig. 10. Power spectra for the local fields and the average field presented in Fig. 9. Note that top and bottom (or left and right) signals have the same spectra.

component at 20 GHz, which corresponds to the slow oscillation in the top figure of Fig. 9. This lower frequency at 20 GHz appears also in the case without index guiding. This frequency and all lower ones are due to relaxation oscillation and due to beatings of the modes at the same order, which would be degenerate for the empty cavity with ideal boundary conditions. We also see from the power spectra that there are two groups of peak frequencies, near 120 and 250 GHz, which indicates that all those patterns belong to modes of up to second order. The time series and spectra shown here should be compared with those in Figs. 4 and 5, where all six data sets show similar behavior in time and frequency domain.

Figure 11 shows snapshots of the field at $J = 1.5 J_0$,

the same value as in the second case of Subsection 3.A. We see that higher-order modes of as many as seven peaks occur. This case should be compared with the case without index guiding, for which only a maximum of two peaks are visible. The time evolution of the local field in this case is quite irregular and will not be shown and discussed further.

Comparing the cases with and without index guiding, we see that more transverse modes are excited at the same level of pumping because of the introduction of index guiding. This result seems to be rather counterintuitive at first. Because the transverse cavity is better defined (or the cavity appears smaller) than in the case without index guiding, one would expect the eigenmodes of the Helmholtz equation to be more densely spaced without index guiding. As a consequence, it should be easier to excite more modes than with index guiding. The answer lies in the modal gain of different modes determined by the overlap integral of different mode functions with carrier density profiles. It has been shown[57] that the threshold gain difference of different modes with index guiding is smaller than without index guiding. This explains why more modes are seen with index guiding.

C. Time-Averaged Near Field
In the experiments that employ direct time-domain near-field measurements[10,11] it is virtually impossible to detect the time evolution of the near field to resolve the multi-mode beating frequencies. Rather, the average near-field patterns are imaged over a period of time that depends on the particular setup. To make the connection with such measurements we consider time-averaged near-field patterns. We choose two time intervals, over which averages are made: 0.138 and 1.38 ns. Figure 12 shows average near-field patterns for the 7.5-μm device at pumping $J = 0.7 J_0$ with (Figs. 12a–12d) and without (Figs. 12e and 12f) index guiding, the same cases consid-
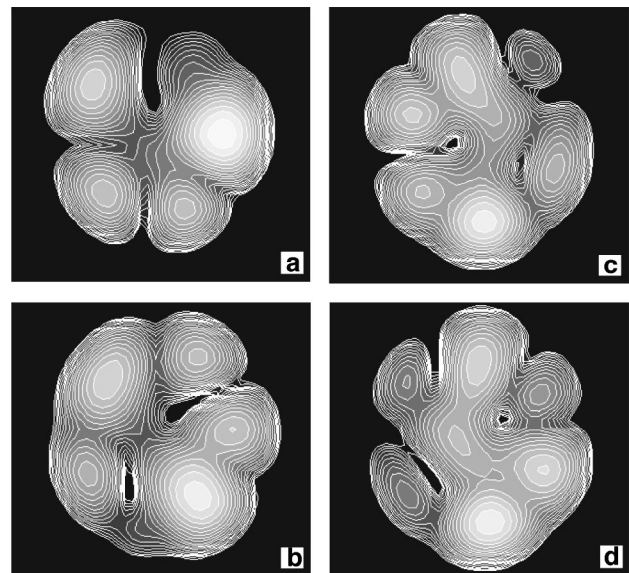

Fig. 11. Snapshots of the near-field patterns at different moments for the gain- and index-guided VCSEL 7.5 μm in diameter at $J = 1.5 J_0$.
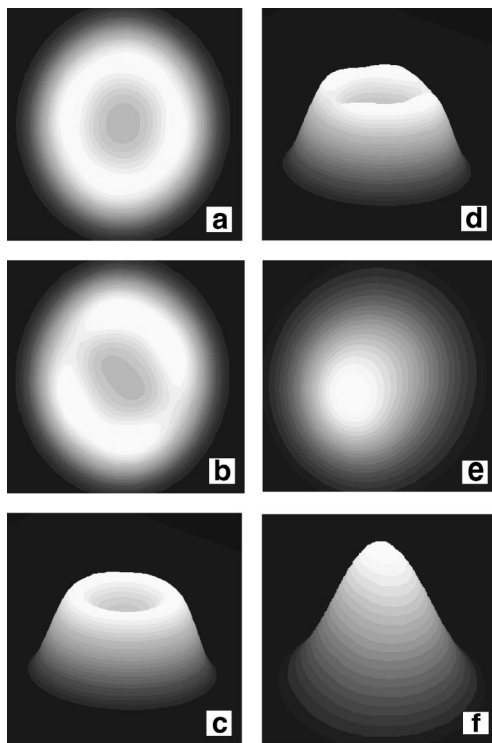
Fig. 12.   Time-averaged near-field patterns with (a–d) and without (e and f) index guiding at $J = 0.7J_0$.   c, d, f, 3D profiles.   b, d, Averaged over 0.138 ns; a, c, averaged over 1.38 ns.

ered in Subsections 3.A and 3.B.   Figures 12a and 12c show the 2D contour and the three-dimensional (3D) profile, respectively, of the near field averaged over 1.38 ns. We can see an almost perfect ring structure in both images.   This structure is steady over a time scale of nanoseconds.   Figures 12b and 12d shows the 2D contour and 3D profile averaged over 0.138 ns.   We see there are some features superimposed upon a ring structure.   Such features rotate on a time scale of a fraction of a nanosecond. On the other hand, the average near field without index guiding shows much different patterns, as shown in Figs. 12e and 12f.   The average field displays a pattern close to the fundamental mode for both averages over 0.138 ns (Figs. 12e and 12f) and over 1.38 ns (not shown).

When the pump is increased to $1.5\,J_0$, the time-averaged near field over 0.138 ns shows a dynamic evolution that involves both zeroth- and first-order modes for the case without index guiding.   This can be seen from Figs. 13a–13c, where the time-averaged field for three successive 0.138-ns time windows is shown.   Figure 13d shows the time-averaged field over 1.38 ns, which is close to zeroth-order mode.   When the index guiding is switched on, the time-averaged field becomes different from that of Fig. 13.   Figures 14a and 14b show the time-averaged fields in this case over 0.138 and 1.38 ns, respectively.   We see a two-ring (a stronger outer ring and a much weaker inner ring) pattern with features superimposed upon both rings.   This pattern is still not stable on this time scale, and it rotates from one time window to the next.   The two-ring structure becomes much more apparent for the average field over 1.38 ns as can be seen from Fig. 14b.

Comparing the time-averaged near field over different time scales with the time-dependent dynamic near field as described in Subsections 3.A and 3.B, we note that the type of pattern that we see depends strongly on the speed of the imaging system used in a particular experiment. Take, for example, the case of an index-guided device at a pumping level of $J = 1.5\,J_0$; the detailed time evolution shows the complicated, high-order mode competition shown in Fig. 11, whereas quite different patterns are seen for the averaged field over 0.138 ns (Fig. 14a) and for that over 1.38 ns (Fig. 14b).   If an imaging system with nanosecond response time were used to study this device, only a ring pattern would be detected, and it might be mistaken as one of the azimuthally symmetrical eigenmodes of a cylindrical cavity.   The case without index guiding is also interesting.   We see that at a pumping level of $J = 1.5\,J_0$ the spatially averaged field and all the local fields at different locations show temporal chaos, as evidenced by the time evolution (Fig. 7a) and the power spectra (Fig. 7b).   But the time-averaged near-field pattern over 1.38 ns is almost exactly the same as the pattern at a pumping level of $J = 0.7J_0$.   We therefore recommend that caution be exercised when connection is made between the near-field image patterns and the pure modes of the Helmholtz equations.   In this respect, we believe that the spatially resolved scanning near-field microscopy spectra provide more-detailed information than the near-field images, and the former should be used to compare with space–time-resolved simulation results.
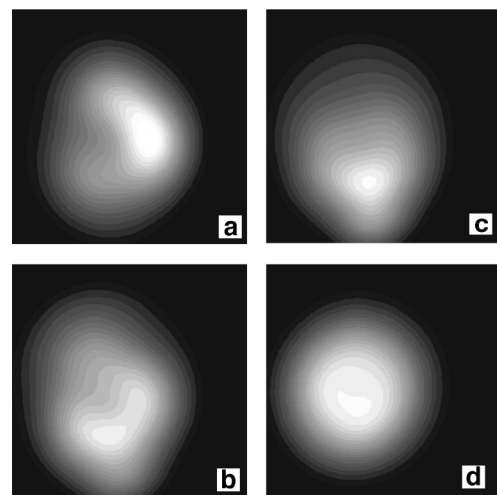

Fig. 13.   Time-averaged near field at $J = 1.5\,J_0$ without index guiding.   a–c, Averaged over 0.138 ns; d, averaged over 1.38 ns.
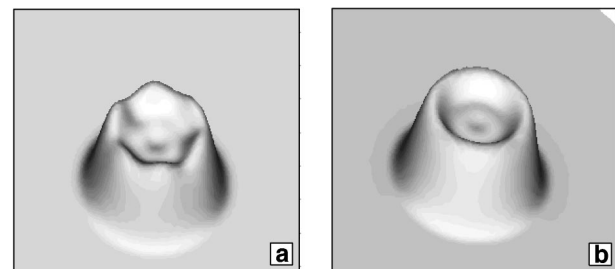

Fig. 14.   3D profiles of the time-averaged near field at $J = 1.5\,J_0$ with index guiding; a and b are averaged over 0.138 and 1.38 ns; respectively.
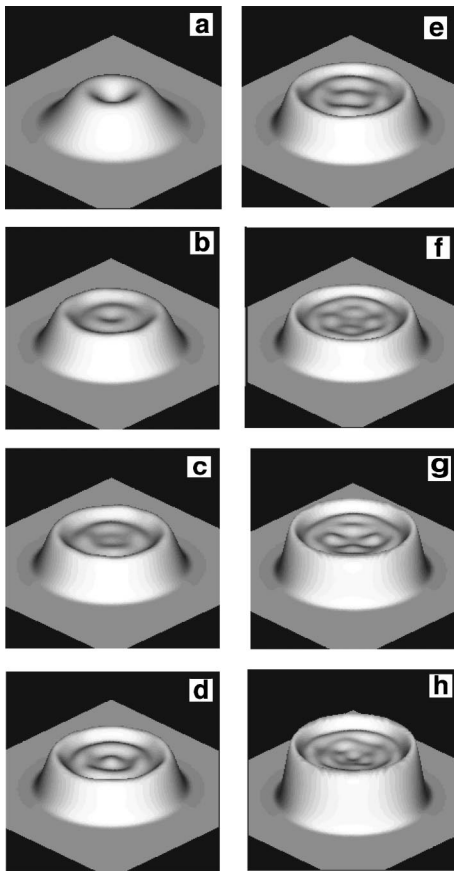
Fig. 15. 3D profiles of the near field for a 15-μm device with index guiding averaged over 1.38 ns. The pumping currents are (from a to h) 0.3, 0.4, 0.5, 0.6, 0.7, 1.0, 1.25, and 1.5 times J_0.

Until now we have dealt with quite small devices, 7.5 μm in diameter. More-complex spatial modes can be seen in larger devices. Figure 15 shows examples of a device 15 μm in diameter with same index-guiding step of 0.05 as in the previous index-guided devices. The detailed time evolution of the field is rather complicated. We focus instead on the long time average of the near field as the pumping current increases. Immediately above threshold, the near field exhibits a stable fundamental mode (not shown). When the pumping is above $0.3J_0$, the device starts showing a dynamic behavior. When the pumping is averaged over 1.38 ns, interesting patterns occur. Figure 15a shows a ring pattern at $0.3J_0$. When the pumping is increased to $0.4J_0$ (Fig. 15b), a second ring appears. This is followed by the appearance of four peaks along the inner ring and a dot in the center at $0.5\,J_0$ (Fig. 15c). With a further increase of pumping to $0.6\,J_0$ (Fig. 15d), the second ring becomes more nearly perfect and the peak at the center becomes stronger. The darker ring around the center peak in Fig. 15d becomes two dips at pumping level $J = 0.7J_0$ (Fig. 15e). Figure 15f shows the pattern at a higher pumping level of $J = J_0$, where we see four peaks surrounded by two rings. This feature becomes more visible with a further increase of pumping at $J = 1.25\,J_0$ (Fig. 15g). At pumping of $1.5\,J_0$ (Fig. 15h), we see features along four different radii, two outer radii that show perfect rings and two inner ones that both show four peaks but rotated 90

deg relative to one and other. It is quite interesting to note that, although the complicated dynamic competition that occurs involves many transverse modes and the corresponding temporal evolution is highly chaotic, the average near field shows the quite regular spatial patterns of Fig. 15.

D. Mode Dynamics in a Ring VCSEL

One of the advantages of VCSEL's is the relative ease of engineering beam shapes through current profiling because of their unique vertical-cavity configuration. Experiments have been carried out to design ring structures to select higher-order transverse modes.[18,19] The flexibility of our simulation code allows us to simulate such ring shapes easily. Here we consider a ring structure with $D_1 = 7$ μm and $D_2 = 15$ μm (see Fig. 2). The structure is, in addition, index guided by use of the same index profile as shown in Fig. 2. Figures 16a–16e shows snapshots of the near field for a pumping of $J = 0.3\,J_0$. The device is slightly above threshold at this pumping level. This ring structure does not seem to have a stable solution. From animation, we see that the near field shows two types of motion. The rotating-wave motion of the eight-peak pattern and the intensity oscillation involves dynamic competition between the eight-peak pattern and a true ring pattern. The eight-peak pattern typically rotates in one direction when the ring pattern is negligibly small. When the ring pattern reaches its maximum and starts to decay, the eight-peak pattern will then change its sense of rotation. Such rotation of the eight-peak pattern, dynamic competition between eight-peak and ring patterns, and rotation reversal persist indefinitely. Figures 16a and 16b show different stages of the rotation.
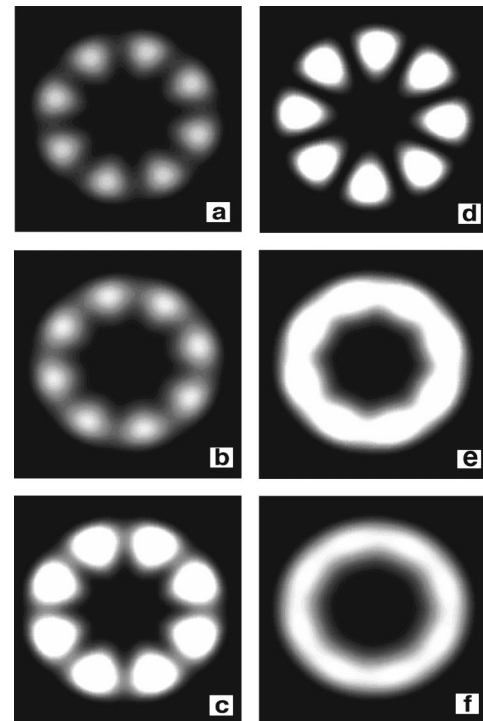

Fig. 16. Contour images of the near field (a–e, snapshots; f, time averaged over 1.38 ns) of a ring VCSEL. Consult text for parameters.

The difference between the two in the brightness of the peaks and of the areas between the peaks indicates the different relative intensities of the ring and the eight-peak patterns at different moments. Figures 16c and 16d show different orientations of the eight-peak pattern when the ring pattern is very small. In fact, the ring pattern has almost completely disappeared in Fig. 16d, where we see that peaks are very well separated. In Fig. 16e, both the ring and the eight-peak patterns reach their maxima, giving a pattern with almost equal amount of each. Figure 16f shows a time average of the near field over 1.38 ns. An almost perfect ring pattern appears, but the eight-peak pattern is still visible. Such multiple peaks, equally spaced along a ring, would be an interesting beam pattern for certain applications, but apparently it is difficult to stabilize them. We are still working on the stabilization of such patterns. On a nanosecond scale, this device provides an almost perfect ring pattern.

4. CONCLUSIONS

We have demonstrated how it is possible to incorporate many-body effects into space–time-domain modeling and simulation of VCSEL's. In principle, one could attempt to solve directly in the space–time domain the partial differential equation version of the semiconductor Bloch equations[48] with all the many-body terms. But such an approach would be too computationally expensive, as was commented on in detail in Ref. 42. Using the effective Bloch equations and a finite-difference method in the space and time domains makes the computation involved readily manageable. In our simulation on a single SGI Octane processor, it takes less than 1 h for a 1-ns simulation. Our simulation code scales quite well with multiple processors. For example, 1-ns simulation takes less than 16 min with four processors of the same machine. Our modeling and simulation are versatile enough to deal with any engineered gain and index confinements or any shapes of current contacts. We believe that such a simulation code could provide a unique tool for comparing theory and simulation with experimental measurements and for designing VCSEL beam profiles for various applications.

To summarize our simulation results, we investigated how the time-resolved and time-averaged field patterns change with increasing pumping current. The two dominant dynamic phenomena that we observed are the rotating-wave patterns and the dynamic competition that often lead to intensity oscillations of different patterns. We see often that the competition between modes of the same order leads to rotating waves, whereas the competition between modes of different orders leads to fast intensity oscillations of the participating modes. We point out that the measured near-field patterns depend on the speed of the particular imaging system. We have also studied the effects of index confinement on the near-field patterns. We found that, in general, index-guided VCSEL's involve more transverse modes than do purely gain-guided devices.

To conclude, we make one final remark: Often the modes of the Helmholtz equation with ideal boundary conditions are used to interpret experimental results or to study the transverse modes of VCSEL's. There are two possible sources of error here. The first one arises from the fact that VCSEL structures usually do not have a simple, well-defined, ideal boundary in the transverse section. This could be due to the carrier-diffusion-induced ramp region or oxidation profile. The second source is the unavoidable time-averaging that is due to the slower detection speed in space–time-domain measurement. For example, in Figs. 13d and 14a, respectively, patterns that look like a fundamental mode or ring mode are observed. But we know that these patterns are superpositions of several different modes at different moments and therefore should be different from the corresponding pure modes of the Helmholtz equation.

REFERENCES

1. For a survey of recent progress in VCSEL's, see C. Chang-Hasnain, ed., *Advances in Vertical Cavity Surface Emitting Lasers*, Vol. 15 of OSA Trends in Optics and Photonics Series (Optical Society of America, Washington, D.C., 1997).
2. W. W. Chow, K. D. Choquette, M. H. Crawford, K. L. Lear, and G. R. Hadley, "Design, fabrication, and performance of infrared and visible vertical-cavity surface-emitting lasers," IEEE J. Quantum Electron. **33**, 1810–1824 (1997).
3. C. J. Chang-Hasnain, J. P. Harbison, G. Hasnain, A. Von Lehmen, L. T. Florez, and N. G. Stoffel, "Dynamic, polarization, and transverse mode characteristics of vertical cavity surface emitting lasers," IEEE J. Quantum Electron. **27**, 1402–1409 (1991).
4. M. Orenstein, Y. Satuby, U. Ben-Ami, and J. P. Harbison, "Transverse modes and lasing characteristics of selectively grown vertical cavity semiconductor lasers," Appl. Phys. Lett. **69**, 1840–1842 (1996).
5. Y. Satuby and M. Orenstein, "Limits of the modulation response of a single-mode proton implanted VCSEL," IEEE Photon. Technol. Lett. **10**, 760–762 (1998).
6. Y. Satuby and M. Orenstein, "Small signal modulation of multitransverse modes vertical-cavity surface-emitting semiconductor lasers," IEEE Photon. Technol. Lett. **10**, 757–759 (1998).
7. R. A. Morgan, G. D. Guth, M. W. Focht, M. T. Asom, K. Kojima, L. E. Rogers, and S. E. Callis, "Transverse mode control of vertical-cavity top-surface-emitting lasers," IEEE Photon. Technol. Lett. **4**, 374–377 (1993).
8. K. Tai, Y. Lai, K. F. Huang, T. C. Huang, T. D. Lee, and C. C. Wu, "Transverse mode emission characteristics of gain-guided surface-emitting lasers," Appl. Phys. Lett. **63**, 2624–2626 (1993).
9. G. C. Wilson, D. M. Kuchta, J. D. Walker, and J. S. Smith, "Spatial hole burning and self-focusing in vertical-cavity surface-emitting laser diodes," Appl. Phys. Lett. **64**, 542–544 (1994).
10. K. H. Hahn, M. R. Tan, Y. M. Houng, and S. Y. Wang, "Large area multitransverse-mode VCSELs for modal noise-reduction in multimode fibre systems," Electron. Lett. **29**, 1482–1483 (1993).

11. C. Mignosi, P. Dowd, L. Raddatz, I. H. White, M. C. Nowell, D. G. Cunningham, M. R. Tan, and S. Y. Wang, "Dynamics of mode partitioning in gain guided GaAs vertical cavity surface emitting lasers," in *Advances in Vertical Cavity Surface Emitting Lasers*, C. Chang-Hasnain, ed., Vol. 15 of OSA Trends in Optics and Photonics Series (Optical Society of America, Washington, D.C., 1997), pp. 77–82.

12. S. P. Hegarty, G. Huyet, J. G. McInerney, K. D. Choquette, K. M. Geib, and H. Q. Hou, "Size dependence of transverse mode structure in oxide-confined vertical-cavity laser diodes," Appl. Phys. Lett. **73**, 596–598 (1998).

13. H. Li, T. Lucas, J. G. McInerney, and R. Morgan, "Transverse modes and patterns of electrically pumped vertical-cavity surface-emitting semiconductor lasers," Chaos Solitons Fractals **4**, 1619–1636 (1994).

14. F. B. de Colstoun, G. Khitrova, A. V. Fedorov, T. R. Nelson, C. Lowry, T. M. Brennan, B. G. Hammons, and P. D. Maker, "Transverse modes, vortices and vertical-cavity surface-emitting lasers," Chaos Solitons Fractals **4**, 1575–1596 (1994).

15. J. Heinrich, E. Zeeb, and K. J. Ebeling, "Transverse mode under external feedback and fiber coupling efficiencies of VCSEL's," IEEE Photon. Technol. Lett. **10**, 1365–1367 (1998).

16. I. Hoersch, R. Kusche, O. Marti, B. Weidl, and K. J. Ebeling, "Spectrally resolved near-field mode imaging of vertical-cavity semiconductor lasers," J. Appl. Phys. **79**, 3831–3834 (1996).

17. J. A. DeAro, K. D. Weston, R. W. Herrick, P. M. Petroff, and S. K. Buratto, "Near-field scanning optical microscopy of cleaved vertical-cavity surface-emitting lasers," Semicond. Sci. Technol. **13**, 1364–1367 (1998).

18. D. L. Huffaker, H. Deng, Q. Deng, and D. G. Deppe, "Ring and stripe oxide-confined vertical-cavity surface-emitting lasers," Appl. Phys. Lett. **69**, 3477–3479 (1996).

19. T. Milster, W. Jiang, E. Walker, D. Burak, P. Claisse, P. Kelly, and R. Binder, "A single-mode high-power vertical cavity surface emitting laser," Appl. Phys. Lett. **72**, 3425–3427 (1998).

20. F. Prati, A. Tesei, L. A. Lugiato, and R. J. Horowicz, "Stable states in surface-emitting semiconductor lasers," Chaos Solitons Fractals **4**, 1637–1654 (1994).

21. A. Valle, "Selection and modulation of high-order transverse modes in vertical-cavity surface-emitting lasers," IEEE J. Quantum Electron. **34**, 1924–1932 (1998).

22. A. Valle, J. Sarma, and K. A. Shore, "Spatial holeburning effects on the dynamics of vertical-cavity surface-emitting laser diodes," IEEE J. Quantum Electron. **31**, 1423–1431 (1995).

23. J. Y. Law and G. P. Agrawal, "Effects of spatial hole burning on gain switching in vertical-cavity surface-emitting lasers," IEEE J. Quantum Electron. **33**, 462–468 (1997).

24. J. Y. Law and G. P. Agrawal, "Feedback-induced chaos and intensity-noise enhancement in vertical-cavity surface-emitting lasers," J. Opt. Soc. Am. B **15**, 562–569 (1998).

25. A. Valle, "High-frequency beam steering induced by switching of high-order transverse modes in vertical-cavity surface-emitting lasers," Appl. Phys. Lett. **73**, 1607–1609 (1998).

26. W. Nakwaski and R. P. Sarzala, "Transverse modes in gain-guided vertical-cavity surface-emitting lasers," Opt. Commun. **148**, 63–69 (1998).

27. M. Noble, J. P. Loehr, and J. A. Lott, "Analysis of microcavity VCSEL lasing modes using a full vector weighted index method," IEEE J. Quantum Electron. **34**, 1890–1903 (1998).

28. M. Noble, J. Shin, K. D. Choquette, J. P. Loehr, J. A. Lott, and Y. Lee, "Calculation and measurements of resonant-mode blueshifts in oxide-apertured VCSELs," IEEE Photon. Technol. Lett. **10**, 475–477 (1998).

29. D. Burak and R. Binder, "Electromagnetic characterization of vertical-cavity surface-emitting lasers based on a vectorial eigenmode calculation," Appl. Phys. Lett. **72**, 891–893 (1998).

30. D. Burak and R. Binder, "Cold-cavity vectorial eigenmodes of VCSELs," IEEE J. Quantum Electron. **33**, 1205–1215 (1997).

31. X. M. Gong, A. K. Chan, and H. F. Taylor, "Lateral mode discrimination in surface emitting DBR lasers with cylindrical symmetry," IEEE J. Quantum Electron. **30**, 1212–1218 (1994).

32. B. Demeulenaere, P. Bienstman, B. Dhoedt, and R. G. Baets, "Detailed study of AlAs-oxidized apertures in VCSEL cavities for optimized model performance," IEEE J. Quantum Electron. **35**, 358–367 (1999).

33. B. Klein, L. F. Register, K. Hess, D. G. Deppe, and Q. Deng, "Self-consistent Green's function approach to the analysis of dielectrically apertured vertical-cavity surface-emitting lasers," Appl. Phys. Lett. **73**, 3324–3326 (1998).

34. H. Wenzel and H.-J. Wünsche, "The effective frequency method in the analysis of vertical-cavity surface-emitting lasers," IEEE J. Quantum Electron. **33**, 1156–1162 (1997).

35. D. Burak, S. A. Kemme, R. K. Kostuk, and R. Binder, "Spectral identification of transverse lasing modes of multiple index-guided vertical-cavity surface-emitting lasers," Appl. Phys. Lett. **73**, 3501–3503 (1998).

36. G. R. Hadley, K. L. Lear, M. E. Warren, K. D. Choquette, J. W. Scott, and S. W. Corzine, "Comprehensive numerical modeling of vertical-cavity surface-emitting lasers," IEEE J. Quantum Electron. **32**, 607–616 (1996).

37. T. Rössler, R. A. Indik, G. K. Harkness, J. V. Moloney, and C. Z. Ning, "Modeling the interplay of thermal effects and transverse mode behavior in native-oxide-confined vertical-cavity surface-emitting lasers," Phys. Rev. A **58**, 3279–3292 (1998).

38. P. M. Goorjian and C. Z. Ning, "Transverse mode dynamics of VCSELs through space–time domain simulation," in *Physics and Simulation of Optoelectronic Devices VII*, P. Blood, A. Ishibashi, and M. Osinski, eds., Proc. SPIE **3625**, 395–403 (1999).

39. C. Z. Ning, S. Bischoff, S. W. Koch, G. K. Harkness, J. V. Moloney, and W. W. Chow, "Microscopic modeling of vertical-cavity surface-emitting lasers: many-body interaction, plasma heating, and transverse dynamics," Opt. Eng. **37**, 1175–1181 (1998).

40. H. Haug and H. Haken, "Theory of noise in semiconductor laser emission," Z. Phys. **204**, 262–275 (1967).

41. C. H. Henry, "Theory of the linewidth of semiconductor lasers," IEEE J. Quantum Electron. **QE-18**, 259–264 (1982).

42. C. Z. Ning, R. A. Indik, and J. V. Moloney, "Effective Bloch equations for semiconductor lasers and amplifiers," IEEE J. Quantum Electron. **33**, 1543–1550 (1997).

43. C. Z. Ning, J. V. Moloney, A. Egan, and R. A. Indik, "A first-principles fully space–time resolved model for a semiconductor laser," Quantum Semiclassic. Opt. **9**, 681–691 (1997).

44. J. V. Moloney, R. A. Indik, and C. Z. Ning, "Full space–time simulation of the high-brightness semiconductor lasers," IEEE Photon. Technol. Lett. **9**, 731–733 (1997).

45. J. V. Moloney, A. Egan, C. Z. Ning, and R. A. Indik, "Spontaneous spatiotemporal instabilities in current modulated master oscillator power amplifier lasers," IEEE Photon. Technol. Lett. **10**, 1229–1231 (1998).

46. A. Egan, C. Z. Ning, J. V. Moloney, R. A. Indik, M. Wright, D. J. Bossert, and J. G. McInerney, "Dynamic instabilities in master oscillator power amplifier semiconductor lasers," IEEE J. Quantum Electron. **34**, 166–170 (1998).

47. P. M. W. Skovgaard, J. G. McInerney, J. V. Moloney, R. A. Indik, and C. Z. Ning, "Enhanced stability of MFA-MOPA semiconductor lasers using a nonlinear, trumpet-shaped flare," IEEE Photon. Technol. Lett. **9**, 1220–1222 (1997).

48. W. W. Chow, S. W. Koch, and M. Sargent, *Semiconductor Laser Physics* (Springer-Verlag, Berlin, 1994), Chap. 4, pp. 119–156.

49. C. Z. Ning, R. A. Indik, J. V. Moloney, W. W. Chow, A. Girndt, S. W. Koch, and R. Binder, "Incorporating many-body effects into modeling of semiconductor lasers and amplifiers," in *Physics and Simulation of Optoelectronic Devices V*, W. W. Chow and M. Osinski, eds., Proc. SPIE **2994**, 666–677 (1997).

50. C. Z. Ning, R. A. Indik, and J. V. Moloney, "Self-consistent approach to thermal effects in vertical-cavity surface-emitting lasers," J. Opt. Soc. Am. B **12**, 1993–2004 (1995).

51. S. Hughes, A. Knorr, S. W. Koch, R. Binder, R. Indik, and J. V. Moloney, "The influence of electron–hole-scattering on the gain spectra of highly excited semiconductors," Solid State Commun. **100**, 555–559 (1996).

52. A. Girndt, F. Jahnke, A. Knorr, S. W. Koch, and W. W. Chow, "Multi-band Bloch equations and gain spectra of highly excited II–VI semiconductor quantum wells," Phys. Status Solidi B **202**, 725–739 (1997).

53. W. W. Chow, A. Knorr, S. Hughes, A. Girndt, and S. W. Koch, "Carrier correlation effects in a quantum well semiconductor laser medium," IEEE J. Sel. Top. Quantum Electron. **3**, 136–141 (1997).

54. J. Yao, G. P. Agrawal, P. Gallion, and C. Bowden, "Semiconductor laser dynamics beyond the rate-equation approximation," Opt. Commun. **119**, 246–255 (1995).

55. W. Yuen, G. S. Li, and C. J. Chang-Hasnain, "Multiple-wavelength vertical-cavity surface-emitting laser arrays with a record wavelength span," IEEE Photon. Technol. Lett. **8**, 4–6 (1996).

56. A. Fiore, Y. A. Akulova, J. Ko, E. R. Hegblom, and L. A. Coldren, "Low-threshold multiple-wavelength vertical-cavity laser arrays obtained by postgrowth wet oxidation," Electron. Lett. **34**, 1857–1858 (1998).

57. R. Michalzik and K. J. Ebeling, "Generalized BV diagrams for higher order transverse modes in planar vertical-cavity laser diodes," IEEE J. Quantum Electron. **31**, 1371–1379 (1995).